

# Prospects of future MeV telescopes in probing weak-scale Dark Matter

---

Marco Cirelli,<sup>a</sup> Arpan Kar<sup>a</sup>

<sup>a</sup>*Laboratoire de Physique Théorique et Hautes Énergies (LPTHE), CNRS & Sorbonne Université,  
4 Place Jussieu, Paris, France*

*E-mail:* [marco.cirelli@gmail.com](mailto:marco.cirelli@gmail.com), [arpankarphys@gmail.com](mailto:arpankarphys@gmail.com)

ABSTRACT: Galactic weak-scale Dark Matter (DM) particles annihilating into lepton-rich channels not only produce gamma-rays via prompt radiation but also generate abundant energetic electrons and positrons, which subsequently emit through bremsstrahlung or inverse Compton scattering (collectively called ‘secondary-radiation photons’). While the prompt gamma-rays concentrate at high-energy, the secondary emission falls in the MeV range, which a number of upcoming experiments (AMEGO, E-ASTROGAM, MAST. . . ) will probe. We investigate the sensitivity of these future telescopes for weak-scale DM, focusing for definiteness on observations of the galactic center. We find that they have the potential of probing a wide region of the DM parameter space which is currently unconstrained. Namely, in rather optimistic configurations, future MeV telescopes could probe thermally-produced DM with a mass up to the TeV range, or GeV DM with an annihilation cross section 2 to 3 orders of magnitude smaller than the current bounds, precisely thanks to the significant leverage provided by their sensitivity to secondary emissions. We comment on astrophysical and methodological uncertainties, and compare with the reach of high-energy gamma ray experiments.

---

## Contents

<b>1</b>	<b>Introduction</b>	<b>1</b>
<b>2</b>	<b>MeV-GeV photons in the Galaxy</b>	<b>3</b>
2.1	Photon signals from DM annihilation in the Galaxy	3
2.1.1	Primary signal: prompt $\gamma$ -ray emission	4
2.1.2	Secondary signal: Inverse Compton Scatterings	4
2.1.3	Secondary signal: bremsstrahlung	7
2.2	Background models and data	8
<b>3</b>	<b>Future MeV telescopes</b>	<b>8</b>
<b>4</b>	<b>Methodology</b>	<b>9</b>
4.1	Conservative upper bounds	9
4.2	Discovery reach of future MeV telescopes	10
4.2.1	Simple signal-to-noise ratio (SNR) method	10
4.2.2	Fisher method	11
<b>5</b>	<b>Results and discussion</b>	<b>11</b>
<b>6</b>	<b>Conclusions</b>	<b>15</b>
<b>A</b>	<b>Impact of astrophysical uncertainties</b>	<b>16</b>
A.1	DM halo profile	16
A.2	ISRF model	17
A.3	Magnetic field model	17
A.4	Effects of full propagation of $e^\pm$ in the Galaxy	18
A.5	Atmospheric backgrounds	19

---

## 1 Introduction

Despite decades of investigation, Dark Matter (DM) remains one of the most pressing unresolved issues in modern cosmology and particle physics [1]. Weak-scale particle Dark Matter (DM), which is here broadly defined as having a mass between a few GeV and tens of TeV's, remains a motivated framework for the solution of the DM problem. This used to be motivated mostly by the fact that several New Physics theories predicted a weak-scale particle with the appropriate properties to play the role of DM. Nowadays, as the promised New Physics has not showed up (at least yet), the motivation mostly shifted to the fact that particles with weak-scale mass and interactions are produced in the right amount in

the early Universe. Weak-scale DM is still therefore the subject of intense searches with many different methods [1].

Indirect Detection (ID) techniques aim at detecting the signals of DM particle annihilations or decays in the Galaxy or in different astrophysical environments. For weak-scale DM, and restricting to the signals in photons, the observables can consist of mainly two things. On one side, high-energy  $\gamma$ -rays are produced directly in the annihilation (or decay) process, hence called *prompt emission*. On the other side, lower-energy X-rays/ $\gamma$ -rays are produced by the electrons and positrons (generated by DM annihilations or decay), in particular via Inverse Compton Scattering (ICS) processes on the ambient light and via bremsstrahlung processes on the galactic gas. These are dubbed *secondary emission*. In most cases, prompt and secondary emissions both exist, and their relative importance depends on the details of the DM model (for instance, lepton-rich annihilation channels will produce abundant  $e^\pm$  and thus a significant ICS signal), on the ambient conditions (for instance, regions of the Galaxy where the ambient light is more intense will be a more favorable target to search for ICS photons) as well as on the sensitivity of the dedicated experiments.

In the past, the prompt emission signal from weak-scale DM received by far most of the attention, although the importance of secondary emission in DM indirect detection searches has been highlighted in a number of studies, see e.g. [2–12] for ICS and [13] for bremsstrahlung. One potential difficulty for detecting secondary emission is the relatively poor sensitivity of past and existing telescopes in the range 0.1-100 MeV, the so-called *MeV gap*. Indeed, secondary photons from weak-scale DM will in general fall in the gap.<sup>1</sup> Fortunately, a number of upcoming or planned MeV telescopes aim at filling this gap [14]. Among them, AMEGO [15–17], E-ASTROGAM [18, 19] and MAST [20] are expected to provide a good sensitivity. Our main goal in this work is to explore the potential that these future MeV telescopes have in constraining weak-scale DM, compared in particular to high-energy  $\gamma$ -ray telescopes.

Recently, a few studies have done work related to this paper. Refs. [21–24] have applied the same principle to another range of DM masses, namely sub-GeV DM. In [25–27] the authors assess the sensitivity of several future MeV telescopes to MeV-GeV DM, including prompt emission only, and [28] considers the case of Primordial Black Hole (PBH) dark matter. In [29] the authors consider secondary emission signals for a specific weak-scale DM model and for a specific target (dwarf galaxies). Our work therefore significantly extends and generalizes these studies.

The remainder of the paper is organized as follows. In section 2 we discuss the MeV-GeV photon fluxes, focusing in particular on the inner galactic region. Section 2.1 provides

---

<sup>1</sup>For instance, we recall that, as a rule of thumb, ICS processes upscatter the ambient photon energy from its initial low value  $E_\gamma^0$  to a final value of up to  $E_\gamma \approx 4\gamma^2 E_\gamma^0$ . Here  $\gamma = E_e/m_e$  is the relativistic factor of the electrons and positrons. Hence a 10 GeV electron will produce a  $\sim 0.15$  MeV hard X-ray when scattering off the CMB ( $E_\gamma^0 \approx 10^{-4}$  eV), or a  $\sim 1.5$  GeV  $\gamma$ -ray when scattering off optical starlight ( $E_\gamma^0 \approx 1$  eV). For bremsstrahlung, the energy of the emitted photon peaks at a fraction of the initial energy of the  $e^\pm$ , typically between 1/10 and 1/2, depending on both the  $e^\pm$  spectrum and on local conditions. See sections 2.1.2 and 2.1.3 for the full treatment.

the discussion on the weak-scale DM-induced photon signals in the MeV-GeV energy range, focusing on the prompt (section 2.1.1) and the secondary (sections 2.1.2 and 2.1.3) emissions. Section 2.2 summarizes different photon backgrounds and data in the MeV-GeV range. In section 3 we briefly review the different near-future space-based MeV telescopes considered in this work. Section 4 details the methodology used to derive the bounds and the projected sensitivities of the MeV telescopes on DM annihilation. We then present and discuss the results of our analysis in section 5. Our conclusions are contained in section 6. Finally, in Appendix A we provide a discussion on the impact of varying different astrophysical ingredients.

## 2 MeV-GeV photons in the Galaxy

The full energy range of the observed photons that we consider here is  $0.1 \text{ MeV} \lesssim E_\gamma \lesssim 100 \text{ GeV}$ , and, in particular, for the future MeV telescopes we use the range  $0.2 \text{ MeV} \lesssim E_\gamma \lesssim 5 \text{ GeV}$  (for which the galactic background models are provided in [27]). As for the target of observation, we consider a disk of  $10^\circ$  radius around the galactic Center (GC) (following [27, 30, 31]), which becomes our region of interest (ROI). Such an angular size of observation is of the same order as the maximum angular width of the upcoming MeV  $\gamma$ -ray telescopes [15, 16]. Below we discuss the possible DM signals as well as the background photons and observed data from this region in our photon energy range of interest.

### 2.1 Photon signals from DM annihilation in the Galaxy

In this work we assume that the origin of the signal is due to the pair-annihilations of a single-component self-conjugate weak-scale DM, that explains the entire observed DM density. We consider the following annihilation channels one at a time, assuming a 100% branching fraction each time:  $\text{DM DM} \rightarrow \mu^+ \mu^-$ ,  $\text{DM DM} \rightarrow e^+ e^-$ ,  $\text{DM DM} \rightarrow b \bar{b}$  and  $\text{DM DM} \rightarrow W^+ W^-$ .

We assume that the density distribution of DM in the halo, for the target region, is described by the NFW profile [32]:

$$\rho_{\text{DM}}(r) = \frac{\rho_0}{\left(\frac{r}{r_s}\right) \left(1 + \frac{r}{r_s}\right)^2}, \quad (2.1)$$

where  $r$  is radial distance from the GC. For the parameters  $\rho_0$  and  $r_s$  we use the values corresponding to the fitted NFW profile parameters (the central values) obtained in [33] for the baryonic model B2; they are similar to the ones used in [27, 31, 34]<sup>2</sup>. In the following, we derive our main results using this NFW profile. However, for comparison we will also consider other choices, see sec. A.1.

As mentioned in the Introduction, for the considered weak-scale DM scenario, the main sources of photon signals from the GC region over the energy range of interest ( $0.1 \text{ MeV} \lesssim E_\gamma \lesssim 100 \text{ GeV}$ ) are the prompt  $\gamma$ -ray emission and the emissions via Inverse

---

<sup>2</sup>We checked that, using the NFW parameters tabulated in [1], our results (i.e., the DM annihilation signals and the corresponding constraints on DM annihilation) change at most by  $\sim 20\%$ .

Compton Scatterings and bremsstrahlung. As we will see, in some cases, the secondary components, especially the ICS, can become more important compared to the primary one over the considered photon energy range. Below we describe the production of these photon signals <sup>3</sup>.

### 2.1.1 Primary signal: prompt $\gamma$ -ray emission

DM annihilation into a given channel (e.g.,  $e^+e^-$ ,  $\mu^+\mu^-$ ,  $b\bar{b}$  or  $W^+W^-$ ) gives rise to the prompt  $\gamma$ -ray flux which at the observer location can be computed as:

$$\frac{d\Phi_{\text{prompt}}}{dE_\gamma d\Omega} = \frac{\langle\sigma v\rangle}{8\pi m_{\text{DM}}^2} \frac{dN_\gamma}{dE_\gamma} \frac{J_{\Delta\Omega}}{\Delta\Omega}, \quad (2.2)$$

where  $\langle\sigma v\rangle$  and  $m_{\text{DM}}$  are the velocity-averaged annihilation cross-section and the mass of the DM, respectively. The distribution  $\frac{dN_\gamma}{dE_\gamma}(E_\gamma, m_{\text{DM}})$  denotes the photon energy spectrum produced per annihilation in the considered annihilation channel. Such a spectrum is determined using the analytical expressions in [22] for  $m_{\text{DM}} < 5$  GeV and using the PPPC4DMID tools [35] for  $m_{\text{DM}} \geq 5$  GeV. Finally, the astrophysical  $J$ -factor for DM annihilation,  $J_{\Delta\Omega}$ , is defined for the observation region  $\Delta\Omega$  as:

$$J_{\Delta\Omega} = \int_{\Delta\Omega} d\Omega \int_{l.o.s.} ds \rho_{\text{DM}}^2(r(s, \theta)). \quad (2.3)$$

Here  $s$  is the line-of-sight (*l.o.s.*) coordinate (with respect to the observer) which is related to the radial and angular distances from the GC,  $r$  and  $\theta$ , as:  $r = \sqrt{s^2 + r_\odot^2 - 2sr_\odot \cos\theta}$ , with  $r_\odot$  being the distance of the Earth from the GC [33].

In fig. 1, the blue curves show the prompt  $\gamma$ -ray fluxes discussed in eq. (2.2) (averaged over the observation region  $\Delta\Omega$ ), for four benchmark values of the DM mass:  $m_{\text{DM}} = 1, 10, 10^2$  and  $10^3$  GeV, considering the NFW DM profile (eq. 2.1) and the DM DM  $\rightarrow \mu^+\mu^-$  annihilation channel with  $\langle\sigma v\rangle$  set at the thermal value  $\langle\sigma v\rangle = 3 \times 10^{-26} \text{ cm}^3\text{s}^{-1}$ .

### 2.1.2 Secondary signal: Inverse Compton Scatterings

We now move to consider the photon fluxes generated due to the ICS of DM-induced  $e^\pm$  off the ambient photon bath, composed of mainly CMB, infrared (IR) and starlight (SL), collectively denoted as the Inter-Stellar Radiation Field (ISRF). The  $e^-/e^+$  population produced by DM annihilations is written in terms of the source function as:

$$Q_e(E_e^S, r) = \frac{\langle\sigma v\rangle}{2m_{\text{DM}}^2} \frac{dN_e}{dE_e^S} \rho_{\text{DM}}^2(r), \quad (2.4)$$

where  $\frac{dN_e}{dE_e^S}(E_e^S, m_{\text{DM}})$  is the energy spectrum of  $e^-/e^+$  sourced by DM annihilation into a given channel. Such spectra are estimated using the analytical expressions in [22] for  $m_{\text{DM}} < 5$  GeV and using the tools in [35] for  $m_{\text{DM}} \geq 5$  GeV.

<sup>3</sup>Apart from these, the production of another secondary photon signal from the In-flight annihilation (IfA) of DM induced positrons is also possible [21]. However, we checked that, in our considered photon energy range, and for our DM scenario, this flux is well suppressed compared to the other types of flux.

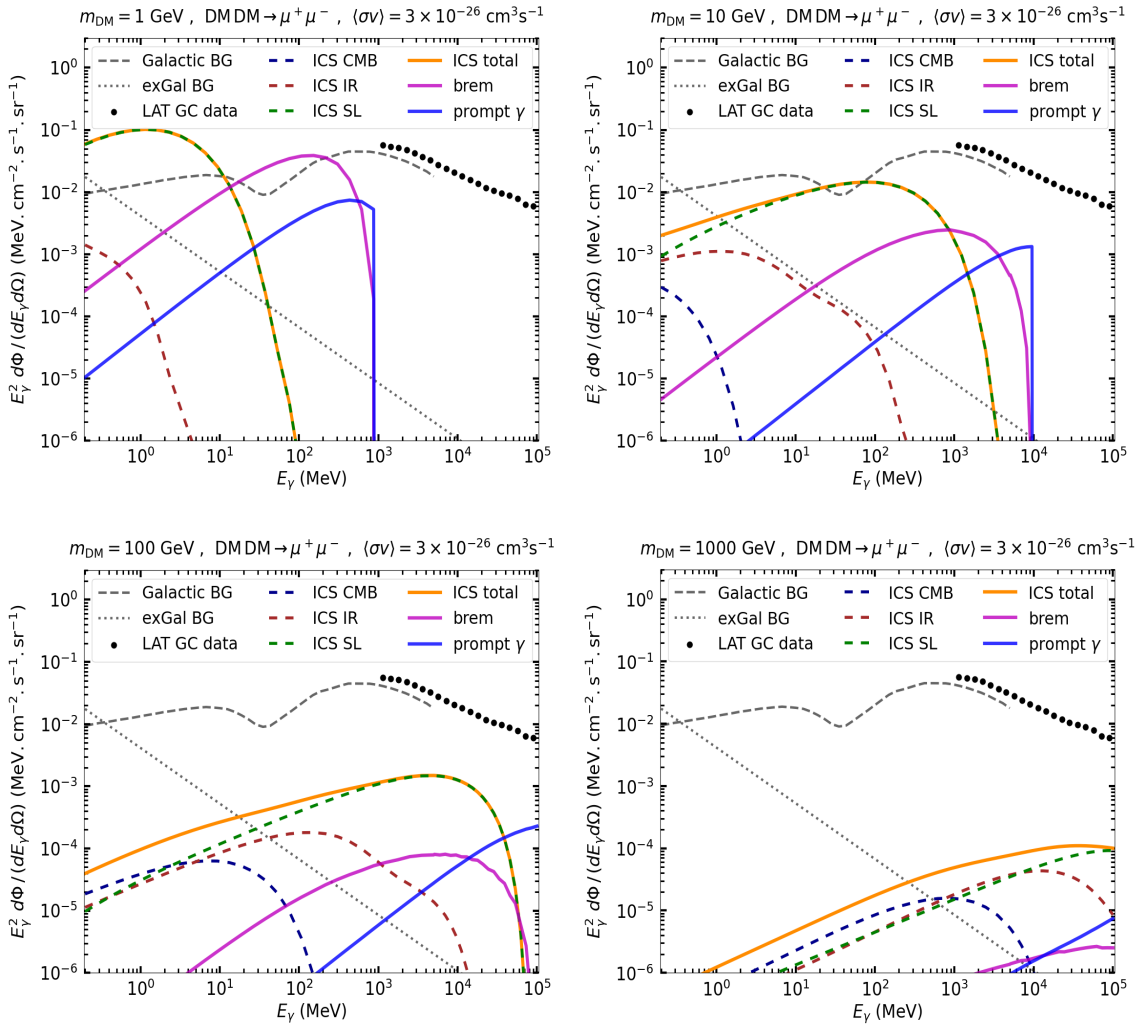


**Figure 1.** *Different types of DM-induced photon fluxes discussed in eqs. (2.2), (2.8) and (2.11), averaged over a disk of  $10^\circ$  around the GC. The four panels are for four different values of the DM mass:  $m_{\text{DM}} = 1, 10, 10^2$  and  $10^3$  GeV. Here, for definiteness, we consider DM DM  $\rightarrow \mu^+ \mu^-$  annihilations with  $\langle \sigma v \rangle = 3 \times 10^{-26} \text{ cm}^3 \text{ s}^{-1}$ . In addition, different diffuse photon backgrounds and the FERMI-LAT GC  $\gamma$ -ray data are also shown (see the text for details). This figure shows that, in our energy range of interest, the secondary photon flux such as the ICS can be a very important component of the DM signal for different DM masses.*

The  $e^\pm$ , after being produced from DM annihilation, propagate through the galactic medium undergoing various effects, such as spatial diffusion, advection, convection, re-acceleration and radiative energy losses, and give rise to a steady state distribution [24, 36, 37]. Since we will be interested in a region of the galactic halo that does not cover the scale of the accretion region of the central black hole, we will assume that the effects of advection and convection can be neglected. On the other hand, near the region around the GC, for  $e^\pm$  with energies above a GeV the effect of energy loss via various radiative processes becomes dominating over other processes, e.g. spatial diffusion and advection

[21]. Also, many of the above-mentioned processes turn out to be more relevant for the propagation of the cosmic-ray nuclei rather than for the  $e^\pm$  (see, e.g., [36, 38] or [1] for a summary). We will therefore adopt here a simplified treatment by assuming that energy losses via various radiative processes dominate the propagation of the DM-induced  $e^\pm$ . This assumption, referred to as the ‘on the spot’ approximation, gives a semi-analytic way to solve the propagation of  $e^\pm$  in the Galaxy. However, in Sec. A.4 we will illustrate the effects caused by considering the full propagation of  $e^\pm$ , and see that the corresponding DM signal from our target region vary at most by a factor of few for the DM mass in the usual GeV–TeV range. A somewhat similar result was previously obtained in [39] and [7, 21, 40].

With the above-mentioned assumption, the spatial and energy distribution of the steady state  $e^\pm$ ’s that give rise to the ICS flux is estimated as [7, 22, 23]:

$$\frac{dn_e}{dE_e}(E_e, \vec{x}) = \frac{1}{b_{\text{tot}}(E_e, \vec{x})} \int_{E_e}^{m_{\text{DM}}} dE_e^S Q_e(E_e^S, r), \quad (2.5)$$

where  $b_{\text{tot}}(E_e, \vec{x})$  is the total energy loss rate of the  $e^\pm$  (having an energy  $E_e$ ) at a position  $\vec{x}$  in the Galaxy. This  $b_{\text{tot}}(E_e, \vec{x})$  includes energy losses of  $e^\pm$  by various radiative processes, i.e. ICS off the ambient photon baths, synchrotron emission in the Galactic magnetic field, Coulomb interactions with the interstellar gases, ionization of the same gases and bremsstrahlung on the same gases. We refer the reader to [41] for their detailed expressions and just remind here that the energy losses through the Coulomb interaction, ionization and bremsstrahlung are more important when the  $e^\pm$  energy  $E_e$  is below a GeV, while for  $E_e$  above a GeV, the losses due to ICS and synchrotron dominate.

Using the  $e^+/e^-$  distribution obtained in eq. (2.5) one can estimate the total ICS emissivity as:

$$j_{\text{ICS}}(E_\gamma, \vec{x}(s, b, l)) = 2 \int_{m_e}^{m_{\text{DM}}} dE_e \sum_{i \in \text{ISRF}} \mathcal{P}_{\text{ICS}}^i(E_\gamma, E_e, \vec{x}) \frac{dn_e}{dE_e}(E_e, \vec{x}), \quad (2.6)$$

where the factor of 2 takes into account the contributions of both electrons and positrons. The coordinates  $(s, b, l)$  correspond to respectively the *l.o.s.* linear coordinate, latitude and longitude of a point with respect to the observer. The angular distance  $\theta$  from the GC is given by  $\cos \theta = \cos b \cos l$ , and the vertical distance above the galactic plane  $z = s \sin b$ . The functions  $\mathcal{P}_{\text{ICS}}^i$  denote the differential power emitted into photons with energy  $E_\gamma$  due to the IC scatterings of an  $e^+/e^-$  (having energy  $E_e$ ) on each ambient photon bath  $i$  in the ISRF (see [1, 3, 7] and Sec. A.2),

$$\mathcal{P}_{\text{ICS}}^i(E_\gamma, E_e, \vec{x}) = c E_\gamma \int d\epsilon n_i^{\text{ISRF}}(\epsilon, \vec{x}) \sigma_{\text{IC}}(\epsilon, E_\gamma, E_e), \quad (2.7)$$

where  $i \rightarrow \text{CMB, IR or SL}$ . The differential photon number density  $n_i^{\text{ISRF}}(\epsilon, \vec{x})$  corresponding to each ISRF component is the same one used in [22]. The quantity  $\sigma_{\text{IC}}$  is the Klein-Nishina cross-section, obtained using the analytical expressions given in [1, 3, 7]. The limit of integration over  $\epsilon$  in eq. (2.7) is determined by the kinematics of the IC scattering  $1 \leq q \leq m_e^2/4E_e^2$ , where  $q \equiv \frac{E_\gamma m_e^2}{4\epsilon E_e(E_e - E_\gamma)}$ . An illustration of  $\mathcal{P}_{\text{ICS}}^i$  (corresponding to the

three ISRF components) as a function of  $E_\gamma$  for different input  $e^\pm$  energies can be found in figure 1 of [22].

Finally, the observable ICS photon flux (averaged over the observation region  $\Delta\Omega$ ) is given by [22, 23]:

$$\frac{d\Phi_{\text{ICS}}}{dE_\gamma d\Omega} = \frac{1}{\Delta\Omega} \int_{\Delta\Omega} d\Omega \left[ \frac{1}{E_\gamma} \int_{l.o.s.} ds \frac{j_{\text{ICS}}(E_\gamma, \vec{x}(s, b, l))}{4\pi} \right]. \quad (2.8)$$

For the spatial integral in the above equation, we cut the distribution of the  $e^\pm$  density in the radial direction at  $R = R_{\text{Gal}} = 20$  kpc, and in the vertical direction at  $z = L_{\text{Gal}} = 4$  kpc, assuming this to be the size of the zone that keeps the  $e^\pm$  confined.

In fig. 1 we plot the ICS photon fluxes (averaged over the observation region), for four values of the DM mass:  $m_{\text{DM}} = 1, 10, 10^2$  and  $10^3$  GeV, considering the DM DM  $\rightarrow \mu^+ \mu^-$  annihilation channel with  $\langle \sigma v \rangle = 3 \times 10^{-26}$  cm<sup>3</sup>s<sup>-1</sup>. We show contributions from different target photons (i.e., from CMB, IR, and SL) separately, together with the sum of all these contributions (the orange solid lines). Fig. 1 shows that, for different DM masses, the DM-induced ICS flux in principle can dominate over the other types of DM-induced signals in our energy range of interest, especially in the low energy regime.

### 2.1.3 Secondary signal: bremsstrahlung

The same  $e^\pm$  populations that produce the ICS flux can also give rise to the bremsstrahlung emission. In analogy with eq. (2.6), the bremsstrahlung emissivity can be expressed as:

$$j_{\text{brem}}(E_\gamma, \vec{x}(s, b, l)) = 2 \int_{m_e}^{m_{\text{DM}}} dE_e \mathcal{P}_{\text{brem}}(E_\gamma, E_e, \vec{x}) \frac{dn_e}{dE_e}(E_e, \vec{x}), \quad (2.9)$$

where the  $e^\pm$  distribution  $\frac{dn_e}{dE_e}(E_e, \vec{x})$  is given by eq. (2.5). The bremsstrahlung power emitted into photons with energy  $E_\gamma$  due to the scattering of an  $e^\pm$  of energy  $E_e$  (with  $E_e > E_\gamma$ ) is given by [41]:

$$\mathcal{P}_{\text{brem}}(E_\gamma, E_e, \vec{x}) = c E_\gamma \sum_i n_i(\vec{x}) \frac{d\sigma_i^{\text{brem}}}{dE_\gamma}(E_e, E_\gamma). \quad (2.10)$$

Here  $n_i(\vec{x})$  describe the number density distribution of each of the gas species (ionic, atomic and molecular) and  $\frac{d\sigma_i^{\text{brem}}}{dE_\gamma}(E_e, E_\gamma)$  is the corresponding differential scattering cross-section for bremsstrahlung. For all the details of these expressions, we refer again the reader to [41].

Finally, the observable photon flux due to bremsstrahlung (averaged over the observation region  $\Delta\Omega$ ) is computed as:

$$\frac{d\Phi_{\text{brem}}}{dE_\gamma d\Omega} = \frac{1}{\Delta\Omega} \int_{\Delta\Omega} d\Omega \left[ \frac{1}{E_\gamma} \int_{l.o.s.} ds \frac{j_{\text{brem}}(E_\gamma, \vec{x}(s, b, l))}{4\pi} \right]. \quad (2.11)$$

The photon fluxes due to the bremsstrahlung emissions arising for different DM masses are shown in fig. 1 by the magenta curves. For our target region, bremsstrahlung emissions can dominate the DM signal in the intermediate part of our energy range of interest, especially when the DM mass is relatively smaller.



## 2.2 Background models and data

The total diffuse photon background towards our target region (i.e., the  $10^\circ$  cone around the GC) receives contributions from both galactic and extra-galactic origins.

The galactic photon backgrounds are obtained from [27] for the energy range  $0.2 \text{ MeV} \lesssim E_\gamma \lesssim 5 \text{ GeV}$ . This is the energy range that we use for the study of future MeV telescopes. The diffuse galactic background model consists of mainly four different astrophysical components. Three of them, namely: a bremsstrahlung component, a  $\pi^0$  component and a high energy ICS component (ICS<sub>hi</sub>), were computed with the GALPROP code [42] and fitted to the FERMI-LAT data at higher energies [43]. The fourth one, another ICS component (ICS<sub>lo</sub>), was modeled as a power-law and fitted to COMPTEL and EGRET data at lower energies [21, 44]. All these background models were presented in [21] for a region  $|l| \leq 5^\circ$ ,  $|b| \leq 5^\circ$  around the GC. Each of these models was then rescaled by [27] to the  $10^\circ$  cone region around the GC and presented in their figure 1. We adopt these models as our fiducial galactic photon backgrounds. On the other hand, for the extra-galactic component, we adopt the single power law model from [28], with their best-fit values of the normalization and the power law index as the fiducial parameters.

In each panel of fig. 1, the total fiducial galactic photon background (the sum of four components listed above) and the fiducial extra-galactic photon background are shown by the gray dashed and dotted lines, respectively. Along with these backgrounds, we also show in each plot with black points the FERMI-LAT  $\gamma$ -ray data towards the GC. These are taken from [45] for a  $15^\circ \times 15^\circ$  region around the GC and presented in this figure by normalizing with respect to the corresponding solid angle.

## 3 Future MeV telescopes

We study the prospects of probing the DM signals in different near-future MeV space telescopes [14], such as AMEGO, E-ASTROGAM and MAST. Apart from these three, there are several other planned or proposed space-based MeV telescopes: for instance, COSI [26], GECCO [46], ADEPT [47], GRAMS [48] and PANGU [49]. These instruments have effective areas which are either smaller or of the same order of magnitude than the three above-mentioned instruments, and therefore are expected to provide comparatively smaller or similar sensitivities for the DM signal searches. We thus choose to focus on AMEGO, E-ASTROGAM and MAST, and give here a brief description of their main properties relevant for DM searches.

- AMEGO: The All-sky Medium Energy Gamma-ray Observatory (AMEGO) is a proposed future space-based mission, poised to provide important contributions to multi-messenger astrophysics in the late 2020's and beyond. It can operate in two different modes, Compton scattering and pair-production modes, to achieve high sensitivity in a wide energy range  $0.2 \text{ MeV}$  to  $\sim 5 \text{ GeV}$ . The Compton mode is divided into two parts: untracked Compton and tracked Compton. By combining three different event classifications it can achieve an effective area of  $\sim 500 - 1000 \text{ cm}^2$  across the full

energy range. A detailed overview of various instrumental details of AMEGO, e.g., effective area, energy resolution and angular resolution for different modes, can be found in Refs. [15, 16]. For our work we use the three effective areas discussed above and an energy resolution of 30% for the full range of energy over which it can operate. There is also a more recent proposal for an instrument, named AMEGO-X [17], with a similar concept.

- E-ASTROGAM: E-ASTROGAM (or enhanced-ASTROGAM) is a satellite gamma-ray mission concept proposed by a wide international community for the late 2020's. Like AMEGO, it can operate in both Compton scattering and pair-production modes to achieve good sensitivity over a broad energy range 0.3 MeV to 3 GeV (the lower energy limit can be pushed to energies as low as 150 keV and 30 keV with improved tracker and calorimetric detections, respectively). Its effective area and energy resolution vary between  $\sim 10^2 - 10^3 \text{ cm}^2$  and  $\mathcal{O}(1)\% - 30\%$ , respectively, in the two modes over the energy range 0.3 MeV - 3 GeV. All the details related to its various instrumentation can be obtained from [18, 19]. In our case, we conservatively consider an energy resolution of 30% over its full energy range.
- MAST: The Massive Argon Space Telescope (MAST) is another proposed future satellite-based telescope that plans to use a liquid Argon time projection chamber for  $\gamma$ -ray astronomy. Compared to the other future telescopes, it has a significantly larger effective area, which is estimated to be approximately  $\sim 10^5 \text{ cm}^2$  over the energy range  $E_\gamma > 10 \text{ MeV}$ . For the instrumental details see [20]. We have considered an energy resolution of 30% for the full energy range of this telescope. The high sensitivity of MAST in searching MeV DM and primordial black hole (PBH) DM signals was discussed in [27, 30, 50] and [31, 51], respectively.

In fig. 2 the effective areas of the various considered future telescopes are shown for the range of the photon energy (0.2 MeV - 5 GeV) considered in this work. See also [27] for a more detailed summary of these telescopes.

## 4 Methodology

In this section we discuss the methodology adopted in this work to obtain the projections of the future MeV telescopes on the DM parameter space. To obtain these projections we consider the sum of ICS (2.8), bremsstrahlung (2.11) and prompt  $\gamma$ -rays (2.2) fluxes discussed in section 2 as the total DM-induced signal.

### 4.1 Conservative upper bounds

Before discussing the projections for the future MeV telescopes, we first derive some simple estimates of the possible upper bounds on the DM annihilation cross-section  $\langle\sigma v\rangle$ , based on existing  $\gamma$ -ray observations (in the range  $0.2 \text{ MeV} \lesssim E_\gamma \lesssim 100 \text{ GeV}$ ).

For each of the considered annihilation channels, we obtain such estimates using the following approach. We require that, for a fixed  $m_{\text{DM}}$ , the total predicted DM photon

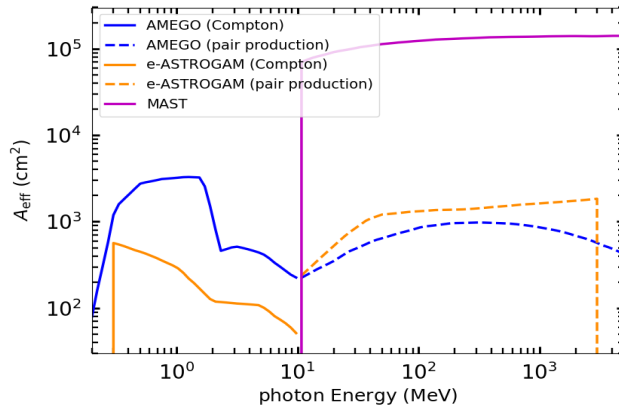


**Figure 2.** *Effective areas* of the future telescopes AMEGO, E-ASTROGAM and MAST, for the range of the photon energy considered in this work.

signal, averaged over the  $10^\circ$  cone around the GC, does not exceed the total fiducial MeV photon background (the sum of the gray dashed and dotted lines from fig. 1, based on EGRET and COMPTEL data as discussed in sec. 2.2) at any energy bin in the range  $0.2 \text{ MeV} \lesssim E_\gamma \lesssim 5 \text{ GeV}$ , as well as the total signal, averaged over the  $15^\circ \times 15^\circ$  region around the GC, does not exceed the FERMI-LAT data (the black points in fig. 1) at any energy bin in the range  $5 \text{ GeV} \lesssim E_\gamma \lesssim 100 \text{ GeV}$ . This leads to an upper bound on  $\langle \sigma v \rangle$  for the given  $m_{\text{DM}}$ . The resulting constraints are drawn with a red solid line in figure 3 below.

## 4.2 Discovery reach of future MeV telescopes

In order to obtain the projected sensitivities or the discovery potentials of the MeV telescopes we take two approaches, discussed below.

### 4.2.1 Simple signal-to-noise ratio (SNR) method

In this case we take the simple approach presented in [30, 31] and require the signal-to-noise ratio (SNR) over the observation time period to be larger than five, i.e.,

$$\frac{N_\gamma|_{\text{DM}}}{\sqrt{N_\gamma|_{\text{BG}}}} \geq 5, \quad (4.1)$$

which leads to a  $\sim 5\sigma$  projection on  $\langle \sigma v \rangle$  for a given  $m_{\text{DM}}$ . Here  $N_\gamma|_{\text{BG}}$  is the photon count of the total diffuse background (sum of the galactic and extra-galactic background components discussed in sec. 2), while  $N_\gamma|_{\text{DM}}$  corresponds to the DM induced total photon signal for a given DM mass. The number of photon count over the energy range  $[E_{\text{min}}, E_{\text{max}}]$  is defined as:

$$N_\gamma = t_{\text{obs}} \int_{E_{\text{min}}}^{E_{\text{max}}} dE_\gamma A_{\text{eff}}(E_\gamma) \int_{\Delta\Omega} d\Omega \frac{d\Phi}{dE_\gamma d\Omega}, \quad (4.2)$$

with

$$\frac{d\Phi}{dE_\gamma d\Omega} = \int dE'_\gamma R_\epsilon(E_\gamma, E'_\gamma) \frac{d\Phi}{dE'_\gamma d\Omega}, \quad (4.3)$$

where  $\frac{d\Phi}{dE_\gamma d\Omega}$  corresponds to either the DM signal or the diffuse background discussed in sec. 2. The function  $R_\epsilon(E_\gamma, E'_\gamma)$  is a gaussian with mean  $E'_\gamma$  and standard deviation  $\epsilon(E'_\gamma)E'_\gamma$  that accounts for the finite energy resolution of the telescope [25, 52]. The energy resolution  $\epsilon$  and the effective area  $A_{\text{eff}}$  of different MeV telescopes used here are discussed in sec. 3. The solid angle  $\Delta\Omega$  corresponds to our ROI, a region of  $10^\circ$  radius from the GC. Note that the sensitivity of the projection scales with the observation time as  $\sqrt{t_{\text{obs}}}$ .

#### 4.2.2 Fisher method

In this case we take an approach similar to the one presented in [27, 34] involving the Fisher matrix method, employed previously in [53]. We define the vector  $\vec{\theta}$  involving the signal and the background parameters:

$$\vec{\theta} = [\Gamma^{\text{SIG}}, \theta_{\text{brem}}^{\text{BG}}, \theta_{\pi^0}^{\text{BG}}, \theta_{\text{ICS}_{\text{hi}}}^{\text{BG}}, \theta_{\text{ICS}_{\text{lo}}}^{\text{BG}}, \theta_{\text{e.g.}}^{\text{BG}}] , \quad (4.4)$$

where  $\Gamma^{\text{SIG}}$  is the normalization of the DM signal (i.e.,  $\langle\sigma v\rangle$  for a fixed  $m_{\text{DM}}$  and a fixed annihilation channel), while  $\theta_i^{\text{BG}}$  denotes the rescaling of the normalization for each background component  $i$  (representing the bremsstrahlung,  $\pi^0$ ,  $\text{ICS}_{\text{hi}}$ ,  $\text{ICS}_{\text{lo}}$  and extra-galactic components) with respect to the fiducial one, discussed in sec. 2.2. The total differential photon flux is defined as:

$$\phi_{\text{tot}}(\vec{\theta}) = \frac{d\Phi^{\text{SIG}}}{dE_\gamma d\Omega}(\Gamma^{\text{SIG}}) + \sum_I \theta_I^{\text{BG}} \left\{ \frac{d\Phi_{\text{BG}}^I}{dE_\gamma d\Omega} \right\}_{\text{fiducial}} , \quad (4.5)$$

with  $\frac{d\Phi}{dE_\gamma d\Omega}$  defined in eq. (4.3). Using these we define the Fisher matrix as:

$$\mathcal{F}_{ij} = t_{\text{obs}} \int_{E_{\text{min}}}^{E_{\text{max}}} dE_\gamma A_{\text{eff}}(E_\gamma) \int_{\Delta\Omega} d\Omega \left( \frac{1}{\phi_{\text{tot}}} \frac{\partial\phi_{\text{tot}}}{\partial\theta_i} \frac{\partial\phi_{\text{tot}}}{\partial\theta_j} \right)_{\vec{\theta}=\vec{\theta}_{\text{fiducial}}} , \quad (4.6)$$

where  $\vec{\theta}_{\text{fiducial}}$  denotes the fiducial parameters with  $(\Gamma^{\text{SIG}})_{\text{fiducial}}$  set to zero, i.e., considering the null hypothesis (no DM signal is present in the data) to be true.  $\mathcal{F}$  here is a  $6 \times 6$  symmetric matrix. The  $2\sigma$  projected upper bound on the signal normalization  $\Gamma^{\text{SIG}}$  is then defined as:

$$\Gamma_{\text{proj}}^{\text{SIG}} = 2 \sqrt{(\mathcal{F}^{-1})_{11}} . \quad (4.7)$$

Here, too, the sensitivity of the projection scales as  $\sqrt{t_{\text{obs}}}$ .

## 5 Results and discussion

In this section we present the bounds and the projected sensitivities of the future MeV telescopes on DM annihilation, derived in this work using the methodology outlined in sec. 4. The main results of this analysis are presented in fig. 3 for the usual weak-scale DM mass range spanning the GeV–TeV scale. We recall that our target of observation is the inner galactic region (see sec. 2) from where the secondary emission components such as the ICS flux are expected to be very high due to the high densities of the ISRF photons (especially the star light (SL)). This helps to increase the reach of the MeV telescopes

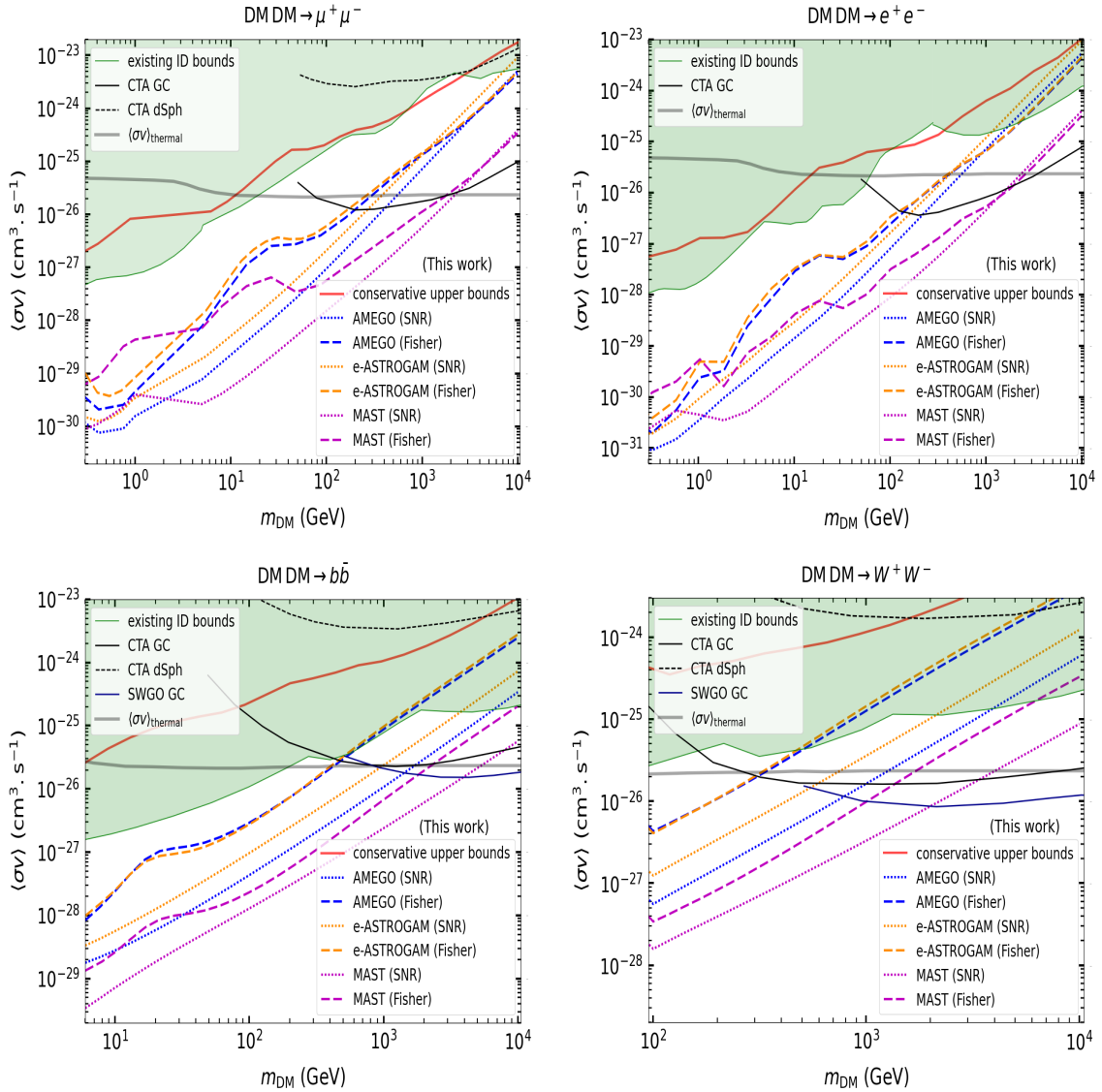


**Figure 3.** *Upper bounds and projected sensitivities on the annihilation cross-section  $\langle\sigma v\rangle$  as a function of  $m_{\text{DM}}$ , for  $\mu^+\mu^-$  (upper left panel),  $e^+e^-$  (upper right panel),  $b\bar{b}$  (bottom left panel) and  $W^+W^-$  (bottom right panel) annihilation channels. Notice the different horizontal and vertical ranges. In each case, our conservative upper bounds are shown with a red solid line, and the existing bounds from the literature with green shaded areas (see the text for details). The projected sensitivities of the upcoming MeV telescopes AMEGO, E-ASTROGAM and MAST are shown by blue, orange and magenta curves, respectively, for an observation time of  $10^8$  sec ( $\simeq 3$  yrs). The solid and dashed black curves show the projections of CTA for the observations towards GC and dwarf galaxies, respectively, and the dark blue curve shows the projection for SWGO, when available. Finally, the solid gray thin band in each plot indicates the value of  $\langle\sigma v\rangle$  corresponding to the observed relic abundance for thermal DM, assuming  $s$ -wave annihilation [54].*

for GeV–TeV DM. The high DM density that one expects in this region also helps. The different astrophysical ingredients used here are the ones discussed in sec. 2. In appendix

A we discuss the variations of such astrophysical ingredients.

The solid red lines in fig. 3 show our estimated upper bounds on  $\langle\sigma v\rangle$  as a function of  $m_{\text{DM}}$ , obtained in sec. 4.1 and corresponding to existing MeV-GeV  $\gamma$ -ray observations, essentially from COMPTEL, EGRET and FERMI-LAT.

Then, for each of the considered DM annihilation channels, we present the projected sensitivities of the upcoming MeV telescopes AMEGO, E-ASTROGAM and MAST with blue, orange and magenta curves, respectively. For each telescope, the dotted and dashed curves correspond to the projections estimated with the two statistical approaches discussed in sections 4.2.1 and 4.2.2, respectively. The observation time  $t_{\text{obs}}$  is assumed to be  $10^8$  sec ( $\simeq 3$  yrs) [30, 31] which is a standard duration achievable by the future MeV telescopes considered here [15–20]. As pointed out earlier, the projected sensitivities scale with the observation time as  $\sqrt{t_{\text{obs}}}$ .

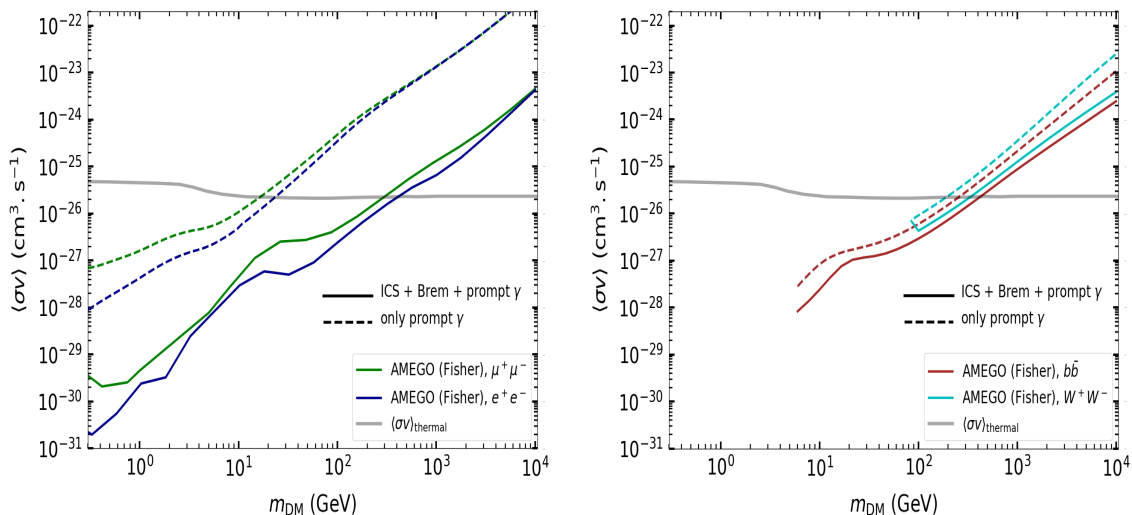


**Figure 4.** Illustration of the *importance of considering the secondary signals* of DM in the case of the leptonic annihilation channels. The comparison between the Fisher projections (for AMEGO with  $t_{\text{obs}} = 10^8$  sec) obtained considering and not considering the secondary signals are shown for the  $\mu^+\mu^-$ ,  $e^+e^-$  (left panel) and the  $b\bar{b}$ ,  $W^+W^-$  (right panel) channels. The colored solid curves are the projections obtained considering the secondary signals and are the same as the ones presented in fig. 3, while the dashed curves show the projections obtained not considering the secondary signals.

We compare our results with the existing bounds (shown by the green shaded areas in fig. 3) obtained from the literature. For a given annihilation channel, these bounds correspond to the most stringent upper limit on  $\langle\sigma v\rangle$  (as a function of  $m_{\text{DM}}$ ) that is compatible with all existing experimental observations. The existing bounds for the  $\mu^+\mu^-$  (for  $m_{\text{DM}} > 5$  GeV),  $b\bar{b}$  and  $W^+W^-$  channels are taken from [1]. For the  $\mu^+\mu^-$  channel, this bound is a combination of limits derived from CMB (assuming  $s$ -wave annihilation) [55, 56], dwarf galaxies  $\gamma$ -rays [57] and ANTARES neutrino [58] observations. On the other hand, for the  $b\bar{b}$  and  $W^+W^-$  channels these bounds are the convolution of limits obtained from dwarf

gamma-rays [59], AMS anti-proton [60] and HESS GC [61, 62] observations. The bounds for  $\mu^+\mu^-$  and  $e^+e^-$  for  $m_{\text{DM}} < 5$  GeV are the combinations of limits from XMM-NEWTON X-ray [23] and CMB ( $s$ -wave) observations. For the  $e^+e^-$  channel, the bound for  $m_{\text{DM}} > 5$  GeV is taken from [63, 64] and it is a convolution of the limits from AMS positron [65, 66], FERMI-LAT dwarfs [67] and HESS GC observations.

Our main result, conveyed by fig. 3, is that, while the upper bounds (the red curves) on  $\langle\sigma v\rangle$  obtained based on the existing  $\gamma$ -ray observations in MeV–GeV range remain mostly within the combined Indirect Detection exclusions (the green shaded regions) discussed above, the future MeV telescopes have the potential to probe large regions of the DM parameter space that are yet unexplored.

Considering the projected sensitivities estimated with the Fisher matrix method, such regions for the  $b\bar{b}$  and  $W^+W^-$  annihilation channels extend up to a few hundreds of GeV (for AMEGO and E-ASTROGAM) or up to a few TeV (for MAST), for thermal DM. For the leptonic channels the forecast sensitivities turn out to be even better. From fig. 3 we see that, for the  $e^+e^-$  and  $\mu^+\mu^-$  channels, the DM parameter space that remains unconstrained but lies within the reach of the future MeV telescopes can be extended up to the TeV or even the multi-TeV mass scale, for thermal DM. Such a statement is in general true for all the MeV telescopes considered here, although MAST is expected to provide a comparatively better sensitivity. Considering a 100 GeV DM annihilating to  $\mu^+\mu^-$ , the Fisher forecasts for AMEGO and E-ASTROGAM reach a value of  $\langle\sigma v\rangle$  which is almost a factor of 30 below the present experimental bound, while for MAST this value can go down by an order of magnitude more.

Taking the rather simplified approach of the signal-to-noise ratio (SNR) method, the estimated sensitivities of the future telescopes extend even further. In fig. 3 this can be seen more prominently for  $m_{\text{DM}} \lesssim 100$  GeV for the  $\mu^+\mu^-$  and  $e^+e^-$  channels, and over all the DM mass range for the  $b\bar{b}$  and  $W^+W^-$  channels.

Among the different MeV telescopes considered here, the forecast sensitivity of MAST turns out to be comparatively better, mainly because of the large effective area estimated for this telescope (see fig. 2). As can be seen from fig. 3, using such an instrument it could be possible to probe in the future a yet unconstrained thermally-annihilating DM model even at the scale of  $\mathcal{O}(10)$  TeV.

MeV telescopes provide a good sensitivity for *leptonic* annihilation channels (like  $\mu^+\mu^-$  and  $e^+e^-$ ) mainly because these channels give rise, through cascades, to copious pairs of  $e^\pm$ , which in the case of usual GeV–TeV scale DM produce strong secondary signals as MeV  $\gamma$ -rays. This is illustrated in fig. 4 (left panel), where the Fisher forecast projections for AMEGO obtained considering the total DM signal are compared to those obtained considering only the prompt  $\gamma$ -ray signals. The prospects for the leptonic channels improve by up to two orders of magnitude when the secondary emission is considered, which shows clearly the importance of including such signals for weak-scale DM. For *hadronic* channels (right panel of fig. 4) the improvement is present but much reduced.

Apart from the MeV  $\gamma$ -ray telescopes, there are various planned and proposed ground-based high-energy  $\gamma$ -ray telescopes such as CTA [68] and SWGO [69], which are also expected to start operating in the forthcoming years. These telescopes are sensitive to  $\gamma$ -rays above  $\sim 50$  GeV. For example, the operating energy range for CTA is 50 GeV – 50 TeV, while for SWGO it is 100 GeV – 1 PeV. As a result, they can also play an important role in probing the annihilations of relatively heavy DM. In fig. 3 we show the projected sensitivities of CTA and SWGO and compare them with those obtained for the MeV telescopes in this work. The solid and dashed black curves show the projections of CTA for the observations towards the GC [70] and the dwarf spheroidal (dSph) galaxy Ursa Major II [71], respectively, for 500 hrs of observation time (that corresponds to  $\sim 5$  yrs of runtime [72]). The dark blue solid curves show the projections of SWGO for the observation towards the GC for 10 yrs [73]. The projections are shown here only for those channels that are available in the corresponding literature. As expected, among different targets, the highest sensitivities of these telescopes are achieved for the observation towards the GC. The high sensitivity of these telescopes for the energetic  $\gamma$ -rays or correspondingly for heavy DM is associated to their large effective areas based on the ground. As can be seen from fig. 3, while these high energy  $\gamma$ -ray telescopes may have a comparatively better sensitivity for a DM mass above a few 100 GeV (when compared to AMEGO or E-ASTROGAM) or a few TeV (when compared to MAST), below such mass ranges the latter class of instruments provide the strongest sensitivities so far in probing DM signals. Therefore, one can say that the future space based MeV  $\gamma$ -ray telescopes will very efficiently complement the ground based high energy  $\gamma$ -ray instruments in the indirect searches for weak-scale DM.

## 6 Conclusions

In this work, we have explored the sensitivity of future MeV telescopes to the photon signals produced by the annihilation of weak-scale DM particles, focusing in particular on the galactic center region. The central idea of our study is that these telescopes will be sensitive to the low-energy secondary emissions (essentially ICS and bremsstrahlung  $\gamma$ -rays produced by the DM-induced electrons and positrons) and will therefore be able to complement the high-energy  $\gamma$ -ray experiments, which are instead insensitive to the DM prompt emission. We focused on three representative planned experiments (AMEGO, E-ASTROGAM and MAST) and on a few representative DM annihilation channels. We adopted for definiteness a NFW DM galactic distribution, a streamlined treatment of the galactic propagation of  $e^\pm$  and standard assumptions for the astrophysical environment (but we investigate in detail the impact of varying all these ingredients in Appendix A). We used two forecast approaches: a simple signal-over-noise ratio criterion and the more refined Fisher matrix method.

Our results are very promising. We find that, thanks to the fact that the secondary emissions significantly enhance the MeV signals of weak-scale DM annihilations, the MeV telescopes will explore a wide area of the  $m_{\text{DM}} - \langle\sigma v\rangle$  parameter space. fig. 3 summarizes our main results. We find that an experiment like MAST, for an observation time of about 3 years, will be able to probe thermally-annihilating DM up to a few TeV's of mass, the



details depending on the annihilation channel and the analysis method. This is comparable to the reach of future high-energy telescopes such as CTA and SWGO. For lower masses, the future MeV telescopes could be sensitive to DM annihilation cross sections that are 2 to 3 orders of magnitude smaller than the current bounds, again with the details depending on the channel and the analysis.

Summarizing, it is remarkable that MeV telescopes will be able to probe TeV DM, possibly competing with TeV telescopes, because of the significant leverage of secondary emissions. This adds an important tool in the continuing quest for the indirect detection of weak-scale DM.

## Acknowledgments

We acknowledge useful discussions with HaoYu Xie. M.C. and A.K. acknowledge the hospitality of the Institut d’Astrophysique de Paris (IAP) where part of this work was done.

Funding and research infrastructure acknowledgments: CNRS grant *DaCo: Dark Connections*; research grant *DaCoSMiG* from the 4EU+ Alliance (including Sorbonne Université).

## A Impact of astrophysical uncertainties

### A.1 DM halo profile

Fig. 5 shows how our results (bounds and projections) vary with different choices for the galactic halo DM profile. The colored solid curves correspond to the NFW profile (eq. (2.1)) with the parameters  $\rho_0$  and  $r_s$  corresponding to the fitted parameters (the central values) obtained in [33] for the baryonic model B2, as used in all other results of this work. The dashed and dashed-dotted curves show, respectively, the results obtained using the Einasto profile [74]

$$\rho_{\text{DM}}^{\text{Ein}}(r) = \rho_0 \exp \left\{ -\frac{2}{\alpha} \left( \left( \frac{r}{r_s} \right)^\alpha - 1 \right) \right\}, \quad (\text{A.1})$$

and a generalized NFW (gNFW) profile

$$\rho_{\text{DM}}^{\text{gNFW}}(r) = \frac{\rho_0}{\left( \frac{r}{r_s} \right)^\gamma \left( 1 + \frac{r}{r_s} \right)^{3-\gamma}}. \quad (\text{A.2})$$

The corresponding profile parameters are set to their central values obtained in the fit in [33] using the same baryonic model B2 used for the NFW profile. The values of  $\alpha$  and  $\gamma$  corresponding to the Einasto and gNFW profiles are  $\alpha = 0.18$  and  $\gamma = 1.3$ , respectively. In fig. 5 we also show, with dotted curves, the results obtained using a truncated isothermal (cored) profile

$$\rho_{\text{DM}}^{\text{Iso}}(r) = \frac{\rho_0}{1 + \left( \frac{r}{r_s} \right)^2}, \quad (\text{A.3})$$

with the corresponding parameters tabulated in [1].

Form fig. 5 we see that, while considering Einasto and gNFW profiles the bounds and projections presented in fig. 3 can strengthen by a factor of 2 and by an order of magnitude, respectively, considering the Isothermal profile they loose by a factor of 10.

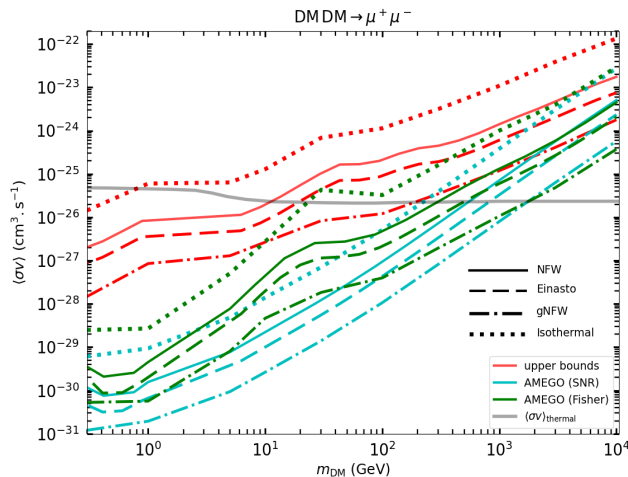


**Figure 5.** Comparison of the bounds and projections (for AMEGO) obtained with *different galactic DM halo profiles*. The colored solid curves correspond to the NFW profile and are the same as the ones shown in fig. 3. The dashed, dashed-dotted and dotted curves correspond to Einasto, generalized NFW (gNFW) and Isothermal profiles, respectively. See the text for details.

## A.2 ISRF model

In fig. 6 we show the DM induced secondary fluxes in the  $\mu^+\mu^-$  annihilation channel for two values of the DM mass,  $m_{\text{DM}} = 1$  GeV (left panel) and 100 GeV (right panel), considering two different ISRF models. The solid curves correspond to the ISRF model discussed in sec. 2.1.2 (which is used in the main results) and are the same as the ones shown in fig. 1. On the other hand, the dashed-dotted curves correspond to the ISRF model “Porter2006” (see [36] for a detailed discussion) that uses the GALPROP dataset [75, 76] and provide an alternative modeling of the radiation fields [77]. This figure shows that using the alternative ISRF model the secondary fluxes change by very small amounts, and mostly for low DM masses. Note from the discussion in sec. 2.1 that the ISRF densities enter into the signal calculation through the ICS emission power as well as through the energy loss of  $e^\pm$ .

## A.3 Magnetic field model

Fig. 7 shows the impact of considering two different Galactic magnetic field models, focusing again on the DM-induced secondary signals in the  $\mu^+\mu^-$  annihilation channel for  $m_{\text{DM}} = 100$  GeV. The solid curves correspond to the model “MF1” (used in the main results) and are the same as the ones presented in fig. 1, while the dashed-dotted curves correspond to the model “MF3” which has a relatively larger strength in the magnetic field. See [41] for a detailed discussion on these models. The latter model causes a (modest) weakening of the DM secondary signal up to a factor of 2, which can be understood as the fact that the  $e^\pm$  lose more energy to synchrotron radiation in the stronger magnetic field (see the discussion in sec. 2.1).

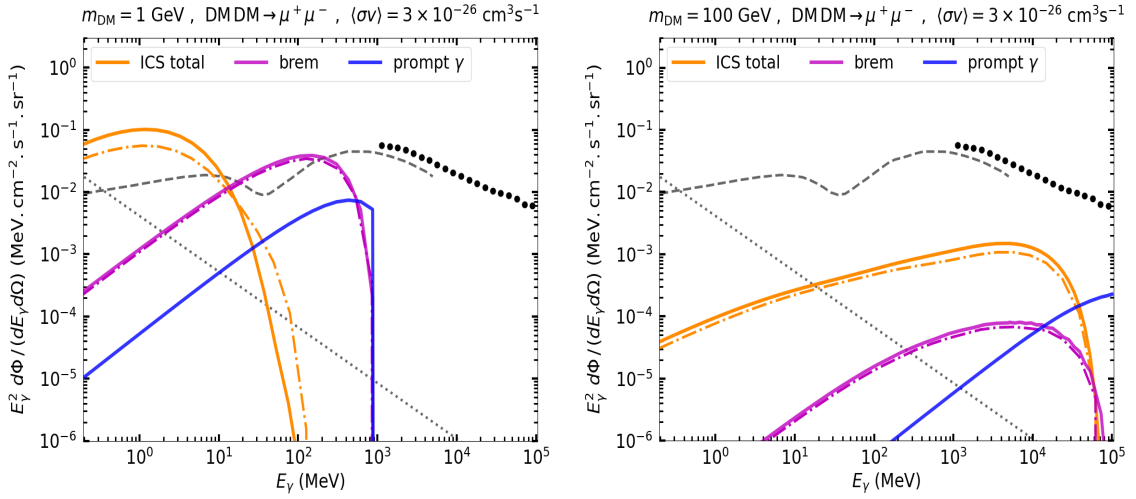


**Figure 6.** *DM-induced photon signals considering different ISRF models.* The dashed-dotted curves (for the ICS and bremsstrahlung signals) are obtained considering the ISRF model “Porter2006” (see [36] for a detailed discussion). The solid curves on the other hand corresponding to the ISRF model discussed in sec. 2.1.2 and are the same as the ones shown in fig. 1.

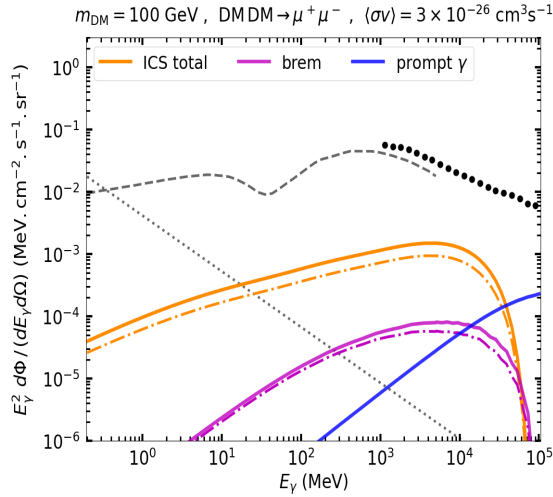


**Figure 7.** *DM-induced signals considering different galactic magnetic field models.* The dashed-dotted curves (for the ICS and bremsstrahlung signals) correspond to the ‘MF3’ model, that is comparatively stronger than the ‘MF1’ model used for the solid curves here and in the main results. See [41] for a detailed discussion on these magnetic field models.

#### A.4 Effects of full propagation of $e^\pm$ in the Galaxy

In fig. 8 we show the effects of considering the full propagation of DM-induced  $e^\pm$  in the Galaxy. These are illustrated for two values of the DM mass,  $m_{\text{DM}} = 1$  GeV and 1000 GeV, considering the  $\mu^+\mu^-$  annihilation channel. The red solid curves correspond to the sum of DM-induced ICS, bremsstrahlung and prompt  $\gamma$ -ray fluxes shown in fig. 1,

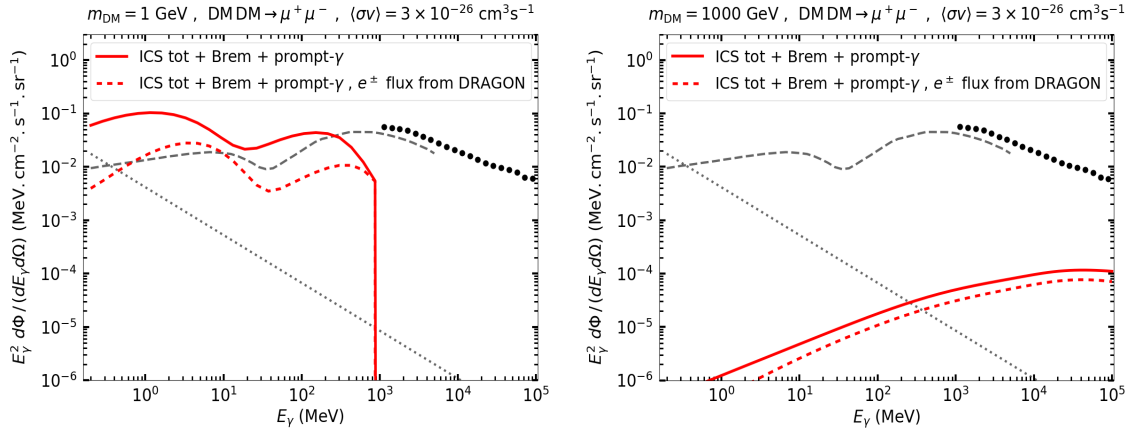
where the  $e^\pm$  distribution required to estimate the secondary signals in the Galaxy were obtained using eq. (2.5). The red dashed curves, on the other hand, correspond to the sum of similar quantities, but the  $e^\pm$  distribution here are obtained by solving the full galactic propagation that includes different processes, such as spatial diffusion, advection, convection, re-acceleration, radiative energy losses and various nuclear processes; see for example eq. 2.1 of [36] or [37]. In order to solve this we use the package DRAGON2 [36, 37]. The spatial diffusion parameters are assumed to be the ones similar to the ‘MAX’ model from [41], but with a smaller thickness ( $\sim 4$  kpc) for the diffusion zone beyond which the  $e^\pm$  escape freely. Note that this ‘MAX’ model, among the different diffusion models studied in [41], provides the largest spatial diffusion coefficient. The Alfvén velocity (related to the re-acceleration of  $e^\pm$ ) and the galactic wind velocity (related to the advection/convection of  $e^\pm$ ) are assumed to be  $v_A = 30$  km/s (which is close to the largest value predicted by cosmic-ray analyses, see [24, 78, 79]) and  $v_w = 250$  km/s (corresponding to a strong wind [21]), respectively. The magnetic field is assumed to be the default model implemented in DRAGON2. The DM profile is considered to be the same one used in fig. 1.

Fig. 8 shows that, across the GeV–TeV DM mass range, the DM signal in the photon energy range of interest can be suppressed at most by a factor  $\lesssim 10$ , if one takes into account the full effects of propagation of  $e^\pm$  in the Galaxy.

Note that we show this figure to illustrate the maximum possible variation in the DM signal one may have by using a detailed and involved numerical simulation of the propagation of charged particles in the Galaxy. The various propagation parameters that are used in this example are conservative. For instance, the choice of the convective wind (which affects mostly the low-energy  $e^\pm$ ) is very large, which is not preferred by recent cosmic-ray analyses [78, 80]. In the absence of the wind the secondary fluxes for low DM masses increase by a factor of a few compared to that obtained considering this wind [21]. Hence, in order to be less dependent on such propagation parameters and to keep full control of our computation, we take the semi-analytic approach described in sec. 2.1 to obtain our main results, and leave a more detailed numerical study involving the full propagation for a future work.

## A.5 Atmospheric backgrounds

Among different future telescopes considered in this work, only E-ASTROGAM so far provides an estimate for the possible atmospheric background (see figure 18 of [18]). Such a background may arise due to various phenomena in the Earth’s atmosphere including the atmospheric lightnings and thunderstorms. In fig. 9 we show an example of the effects of the inclusion of this atmospheric background in the analysis. For the methodology to include such a background we follow [27]. As can be seen, for E-ASTROGAM the effects of the inclusion of the atmospheric background should be mild.



**Figure 8.** *Effects of the propagation of  $e^\pm$ .* The solid curves correspond to the total photon flux (ICS + Brem + prompt- $\gamma$ ) shown in fig. 1. The dashed curves show the same total photon flux, now computed with the  $e^\pm$  distribution in the Galaxy resulting from solving the full propagation equation with DRAGON2 [36, 37].

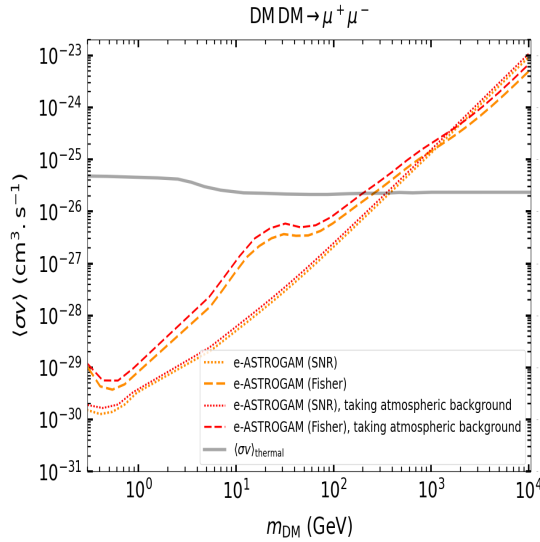


**Figure 9.** *Effects of the inclusion of the possible atmospheric background for E-ASTROGAM.* The red curves are obtained by taking into account the atmospheric background estimated in [18], while the orange curves do not consider this and are the same as the ones shown in fig. 3.

## References

- [1] M. Cirelli, A. Strumia and J. Zupan, *Dark Matter*, [2406.01705](#).
- [2] E. A. Baltz and L. Wai, *Diffuse inverse Compton and synchrotron emission from dark matter annihilations in galactic satellites*, *Phys. Rev. D* **70** (2004) 023512, [[astro-ph/0403528](#)].
- [3] S. Colafrancesco, S. Profumo and P. Ullio, *Multi-frequency analysis of neutralino dark matter annihilations in the Coma cluster*, *Astron. Astrophys.* **455** (2006) 21, [[astro-ph/0507575](#)].
- [4] S. Colafrancesco, S. Profumo and P. Ullio, *Detecting dark matter WIMPs in the Draco*

- dwarf: A multi-wavelength perspective*, *Phys. Rev. D* **75** (2007) 023513, [[astro-ph/0607073](#)].
- [5] I. Cholis, G. Dobler, D. P. Finkbeiner, L. Goodenough and N. Weiner, *The Case for a 700+ GeV WIMP: Cosmic Ray Spectra from ATIC and PAMELA*, *Phys. Rev. D* **80** (2009) 123518, [[0811.3641](#)].
- [6] J. Zhang, X.-J. Bi, J. Liu, S.-M. Liu, P.-F. Yin, Q. Yuan et al., *Discriminating different scenarios to account for the cosmic  $e + / -$  excess by synchrotron and inverse Compton radiation*, *Phys. Rev. D* **80** (2009) 023007, [[0812.0522](#)].
- [7] M. Cirelli and P. Panci, *Inverse Compton constraints on the Dark Matter  $e+e-$  excesses*, *Nucl. Phys. B* **821** (2009) 399–416, [[0904.3830](#)].
- [8] E. Borriello, A. Cuoco and G. Miele, *Secondary radiation from the Pamela/ATIC excess and relevance for Fermi*, *Astrophys. J. Lett.* **699** (2009) L59–L63, [[0903.1852](#)].
- [9] V. Barger, Y. Gao, W. Y. Keung, D. Marfatia and G. Shaughnessy, *Dark matter and pulsar signals for Fermi LAT, PAMELA, ATIC, HESS and WMAP data*, *Phys. Lett. B* **678** (2009) 283–292, [[0904.2001](#)].
- [10] M. Cirelli, P. Panci and P. D. Serpico, *Diffuse gamma ray constraints on annihilating or decaying Dark Matter after Fermi*, *Nucl. Phys. B* **840** (2010) 284–303, [[0912.0663](#)].
- [11] J. Zavala, M. Vogelsberger, T. R. Slatyer, A. Loeb and V. Springel, *The cosmic X-ray and gamma-ray background from dark matter annihilation*, *Phys. Rev. D* **83** (2011) 123513, [[1103.0776](#)].
- [12] G. Beck and S. Colafrancesco, *A Multi-frequency analysis of dark matter annihilation interpretations of recent anti-particle and  $\gamma$ -ray excesses in cosmic structures*, *JCAP* **05** (2016) 013, [[1508.01386](#)].
- [13] M. Cirelli, P. D. Serpico and G. Zaharijas, *Bremsstrahlung gamma rays from light Dark Matter*, *JCAP* **11** (2013) 035, [[1307.7152](#)].
- [14] K. Engel et al., *The Future of Gamma-Ray Experiments in the MeV-EeV Range*, in *Snowmass 2021*, 3, 2022, [[2203.07360](#)].
- [15] AMEGO collaboration, R. Caputo et al., *All-sky Medium Energy Gamma-ray Observatory: Exploring the Extreme Multimessenger Universe*, [[1907.07558](#)].
- [16] C. A. Kierans, *AMEGO: exploring the extreme multimessenger universe*, in *Space Telescopes and Instrumentation 2020: Ultraviolet to Gamma Ray* (J.-W. A. den Herder, S. Nikzad and K. Nakazawa, eds.), vol. 11444 of *Society of Photo-Optical Instrumentation Engineers (SPIE) Conference Series*, p. 1144431, Dec., 2020, [[2101.03105](#)], DOI.
- [17] R. Caputo et al., *All-sky Medium Energy Gamma-ray Observatory eXplorer mission concept*, *J. Astron. Telesc. Instrum. Syst.* **8** (2022) 044003, [[2208.04990](#)].
- [18] e-ASTROGAM collaboration, A. De Angelis et al., *The e-ASTROGAM mission*, *Exper. Astron.* **44** (2017) 25–82, [[1611.02232](#)].
- [19] e-ASTROGAM collaboration, M. Tavani et al., *Science with e-ASTROGAM: A space mission for MeV–GeV gamma-ray astrophysics*, *JHEAp* **19** (2018) 1–106, [[1711.01265](#)].
- [20] T. Dzhatdov and E. Podlesnyi, *Massive Argon Space Telescope (MAST): A concept of heavy time projection chamber for  $\gamma$ -ray astronomy in the 100 MeV–1 TeV energy range*, *Astropart. Phys.* **112** (2019) 1–7, [[1902.01491](#)].

- [21] R. Bartels, D. Gaggero and C. Weniger, *Prospects for indirect dark matter searches with MeV photons*, *JCAP* **05** (2017) 001, [[1703.02546](#)].
- [22] M. Cirelli, N. Fornengo, B. J. Kavanagh and E. Pinetti, *Integral X-ray constraints on sub-GeV Dark Matter*, *Phys. Rev. D* **103** (2021) 063022, [[2007.11493](#)].
- [23] M. Cirelli, N. Fornengo, J. Koechler, E. Pinetti and B. M. Roach, *Putting all the X in one basket: Updated X-ray constraints on sub-GeV Dark Matter*, *JCAP* **07** (2023) 026, [[2303.08854](#)].
- [24] P. De la Torre Luque, S. Balaji and J. Koechler, *Importance of Cosmic-Ray Propagation on Sub-GeV Dark Matter Constraints*, *Astrophys. J.* **968** (2024) 46, [[2311.04979](#)].
- [25] K. K. Boddy and J. Kumar, *Indirect Detection of Dark Matter Using MeV-Range Gamma-Ray Telescopes*, *Phys. Rev. D* **92** (2015) 023533, [[1504.04024](#)].
- [26] A. Caputo, M. Negro, M. Regis and M. Taoso, *Dark matter prospects with COSI: ALPs, PBHs and sub-GeV dark matter*, *JCAP* **02** (2023) 006, [[2210.09310](#)].
- [27] K. E. O'Donnell and T. R. Slatyer, *Constraints on Dark Matter with Future MeV Gamma-Ray Telescopes*, [2411.00087](#).
- [28] A. Ray, R. Laha, J. B. Muñoz and R. Caputo, *Near future MeV telescopes can discover asteroid-mass primordial black hole dark matter*, *Phys. Rev. D* **104** (2021) 023516, [[2102.06714](#)].
- [29] L. Eisenberger, T. Siegert, K. Mannheim and W. Porod, *MHz to TeV expectations from scotogenic WIMP dark matter*, *Mon. Not. Roy. Astron. Soc.* **529** (2024) 1271–1282, [[2310.10421](#)].
- [30] A. Coogan, L. Morrison and S. Profumo, *Precision gamma-ray constraints for sub-GeV dark matter models*, *JCAP* **08** (2021) 044, [[2104.06168](#)].
- [31] A. Coogan, L. Morrison and S. Profumo, *Direct Detection of Hawking Radiation from Asteroid-Mass Primordial Black Holes*, *Phys. Rev. Lett.* **126** (2021) 171101, [[2010.04797](#)].
- [32] J. F. Navarro, C. S. Frenk and S. D. M. White, *The Structure of cold dark matter halos*, *Astrophys. J.* **462** (1996) 563–575, [[astro-ph/9508025](#)].
- [33] P. F. de Salas, K. Malhan, K. Freese, K. Hattori and M. Valluri, *On the estimation of the local dark matter density using the rotation curve of the Milky Way*, *JCAP* **2019** (Oct., 2019) 037, [[1906.06133](#)].
- [34] A. Coogan et al., *Hunting for dark matter and new physics with GECCO*, *Phys. Rev. D* **107** (2023) 023022, [[2101.10370](#)].
- [35] [www.marcocirelli.net/PPPC4DMID.html](http://www.marcocirelli.net/PPPC4DMID.html).
- [36] C. Evoli, D. Gaggero, A. Vittino, G. Di Bernardo, M. Di Mauro, A. Ligorini et al., *Cosmic-ray propagation with DRAGON2: I. numerical solver and astrophysical ingredients*, *JCAP* **02** (2017) 015, [[1607.07886](#)].
- [37] C. Evoli, D. Gaggero, A. Vittino, M. Di Mauro, D. Grasso and M. N. Mazziotta, *Cosmic-ray propagation with DRAGON2: II. Nuclear interactions with the interstellar gas*, *JCAP* **07** (2018) 006, [[1711.09616](#)].
- [38] T. Delahaye, F. Donato, N. Fornengo, J. Lavalle, R. Lineros, P. Salati et al., *Galactic secondary positron flux at the Earth*, *Astron. Astrophys.* **501** (2009) 821–833, [[0809.5268](#)].

- [39] M. Di Mauro and M. W. Winkler, *Multimessenger constraints on the dark matter interpretation of the Fermi-LAT Galactic center excess*, *Phys. Rev. D* **103** (2021) 123005, [[2101.11027](#)].
- [40] P. Meade, M. Papucci, A. Strumia and T. Volansky, *Dark Matter Interpretations of the  $e^+$ -Excesses after FERMI*, *Nucl. Phys. B* **831** (2010) 178–203, [[0905.0480](#)].
- [41] J. Buch, M. Cirelli, G. Giesen and M. Taoso, *PPPC 4 DM secondary: A Poor Particle Physicist Cookbook for secondary radiation from Dark Matter*, *JCAP* **09** (2015) 037, [[1505.01049](#)].
- [42] A. W. Strong and I. V. Moskalenko, *Propagation of cosmic-ray nucleons in the galaxy*, *Astrophys. J.* **509** (1998) 212–228, [[astro-ph/9807150](#)].
- [43] A. W. Strong, *Interstellar Gamma Rays and Cosmic Rays: New Insights from Fermi-Lat and Integral*, in *Cosmic Rays for Particle and Astroparticle Physics* (S. Giani, C. Leroy and P. G. Rancoita, eds.), pp. 473–481, June, 2011, [1101.1381](#), DOI.
- [44] J. F. Beacom and H. Yuksel, *Stringent constraint on galactic positron production*, *Phys. Rev. Lett.* **97** (2006) 071102, [[astro-ph/0512411](#)].
- [45] FERMI-LAT collaboration, M. Ajello et al., *Fermi-LAT Observations of High-Energy  $\gamma$ -Ray Emission Toward the Galactic Center*, *Astrophys. J.* **819** (2016) 44, [[1511.02938](#)].
- [46] E. Orlando et al., *Exploring the MeV sky with a combined coded mask and Compton telescope: the Galactic Explorer with a Coded aperture mask Compton telescope (GECCO)*, *JCAP* **07** (2022) 036, [[2112.07190](#)].
- [47] S. D. Hunter et al., *A Pair Production Telescope for Medium-Energy Gamma-Ray Polarimetry*, *Astropart. Phys.* **59** (2014) 18–28, [[1311.2059](#)].
- [48] T. Aramaki, K. Aoyama, J. Asaadi, L. Fabris, Y. Ichinohe, Y. Inoue et al., *Overview of the GRAMS (Gamma-Ray AntiMatter Survey) Project*, *PoS ICRC2021* (2021) 653.
- [49] X. Wu, M. Su, A. Bravar, J. Chang, Y. Fan, M. Pohl et al., *PANGU: A High Resolution Gamma-ray Space Telescope*, *Proc. SPIE Int. Soc. Opt. Eng.* **9144** (2014) 91440F, [[1407.0710](#)].
- [50] A. Berlin, G. Krnjaic and E. Pinetti, *Reviving MeV-GeV indirect detection with inelastic dark matter*, *Phys. Rev. D* **110** (2024) 035015, [[2311.00032](#)].
- [51] J. Auffinger, *Limits on primordial black holes detectability with Isatis: a BlackHawk tool*, *Eur. Phys. J. C* **82** (2022) 384, [[2201.01265](#)].
- [52] M. Perelstein and B. Shakya, *Dark Matter Identification with Gamma Rays from Dwarf Galaxies*, *JCAP* **10** (2010) 016, [[1007.0018](#)].
- [53] T. D. P. Edwards and C. Weniger, *A Fresh Approach to Forecasting in Astroparticle Physics and Dark Matter Searches*, *JCAP* **02** (2018) 021, [[1704.05458](#)].
- [54] G. Steigman, B. Dasgupta and J. F. Beacom, *Precise Relic WIMP Abundance and its Impact on Searches for Dark Matter Annihilation*, *Phys. Rev. D* **86** (2012) 023506, [[1204.3622](#)].
- [55] T. R. Slatyer, *Indirect dark matter signatures in the cosmic dark ages. I. Generalizing the bound on  $s$ -wave dark matter annihilation from Planck results*, *Phys. Rev. D* **93** (2016) 023527, [[1506.03811](#)].
- [56] L. Lopez-Honorez, O. Mena, S. Palomares-Ruiz and A. C. Vincent, *Constraints on dark matter annihilation from CMB observations before Planck*, *JCAP* **07** (2013) 046, [[1303.5094](#)].



- [57] MAGIC, FERMI-LAT collaboration, M. L. Ahnen et al., *Limits to Dark Matter Annihilation Cross-Section from a Combined Analysis of MAGIC and Fermi-LAT Observations of Dwarf Satellite Galaxies*, *JCAP* **02** (2016) 039, [[1601.06590](#)].
- [58] A. Albert et al., *Results from the search for dark matter in the Milky Way with 9 years of data of the ANTARES neutrino telescope*, *Phys. Lett. B* **769** (2017) 249–254, [[1612.04595](#)].
- [59] HESS, HAWC, VERITAS, MAGIC, H.E.S.S., FERMI-LAT collaboration, H. Abdalla et al., *Combined dark matter searches towards dwarf spheroidal galaxies with Fermi-LAT, HAWC, H.E.S.S., MAGIC, and VERITAS*, *PoS ICRC2021* (2021) 528, [[2108.13646](#)].
- [60] F. Calore, M. Cirelli, L. Derome, Y. Genolini, D. Maurin, P. Salati et al., *AMS-02 antiprotons and dark matter: Trimmed hints and robust bounds*, *SciPost Phys.* **12** (2022) 163, [[2202.03076](#)].
- [61] H.E.S.S. collaboration, H. Abdallah et al., *Search for dark matter annihilations towards the inner Galactic halo from 10 years of observations with H.E.S.S.*, *Phys. Rev. Lett.* **117** (2016) 111301, [[1607.08142](#)].
- [62] H.E.S.S. collaboration, H. Abdalla et al., *Search for Dark Matter Annihilation Signals in the H.E.S.S. Inner Galaxy Survey*, *Phys. Rev. Lett.* **129** (2022) 111101, [[2207.10471](#)].
- [63] R. K. Leane, T. R. Slatyer, J. F. Beacom and K. C. Y. Ng, *GeV-scale thermal WIMPs: Not even slightly ruled out*, *Phys. Rev. D* **98** (2018) 023016, [[1805.10305](#)].
- [64] K. Dutta, A. Ghosh, A. Kar and B. Mukhopadhyaya, *MeV to multi-TeV thermal WIMPs: most conservative limits*, *JCAP* **08** (2023) 071, [[2212.09795](#)].
- [65] AMS COLLABORATION collaboration, M. Aguilar, D. Aisa, A. Alvino, G. Ambrosi, K. Andeen, L. Arruda et al., *Electron and positron fluxes in primary cosmic rays measured with the alpha magnetic spectrometer on the international space station*, *Phys. Rev. Lett.* **113** (Sep, 2014) 121102.
- [66] AMS COLLABORATION collaboration, M. Aguilar, L. Ali Cavazonza, G. Ambrosi, L. Arruda, N. Attig, P. Azzarello et al., *Towards understanding the origin of cosmic-ray positrons*, *Phys. Rev. Lett.* **122** (Jan, 2019) 041102.
- [67] FERMI-LAT, DES collaboration, A. Albert et al., *Searching for Dark Matter Annihilation in Recently Discovered Milky Way Satellites with Fermi-LAT*, *Astrophys. J.* **834** (2017) 110, [[1611.03184](#)].
- [68] K. Bernlöhner, A. Barnacka, Y. Becherini, O. Blanch Bigas, E. Carmona, P. Colin et al., *Monte Carlo design studies for the Cherenkov Telescope Array*, *Astroparticle Physics* **43** (Mar., 2013) 171–188, [[1210.3503](#)].
- [69] A. Albert et al., *Science Case for a Wide Field-of-View Very-High-Energy Gamma-Ray Observatory in the Southern Hemisphere*, [1902.08429](#).
- [70] V. Lefranc, E. Moulin, P. Panci and J. Silk, *Prospects for Annihilating Dark Matter in the inner Galactic halo by the Cherenkov Telescope Array*, *Phys. Rev. D* **91** (2015) 122003, [[1502.05064](#)].
- [71] V. Lefranc, G. A. Mamon and P. Panci, *Prospects for annihilating Dark Matter towards Milky Way’s dwarf galaxies by the Cherenkov Telescope Array*, *JCAP* **09** (2016) 021, [[1605.02793](#)].
- [72] N. L. Rodd, B. R. Safdi and W. L. Xu, *Cta and swgo can discover higgsino dark matter annihilation*, *Phys. Rev. D* **110** (Aug, 2024) 043003.

- [73] A. Viana, H. Schoorlemmer, A. Albert, V. de Souza, J. P. Harding and J. Hinton, *Searching for Dark Matter in the Galactic Halo with a Wide Field of View TeV Gamma-ray Observatory in the Southern Hemisphere*, *JCAP* **12** (2019) 061, [[1906.03353](#)].
- [74] J. Einasto, *On the Construction of a Composite Model for the Galaxy and on the Determination of the System of Galactic Parameters*, *Trudy Astrofizicheskogo Instituta Alma-Ata* **5** (Jan., 1965) 87–100.
- [75] M. Ackermann, M. Ajello, W. B. Atwood, L. Baldini, J. Ballet, G. Barbiellini et al., *Fermi-LAT Observations of the Diffuse  $\gamma$ -Ray Emission: Implications for Cosmic Rays and the Interstellar Medium*, *ApJ* **750** (May, 2012) 3, [[1202.4039](#)].
- [76] A. E. Vladimirov, G. Jóhannesson, I. V. Moskalenko and T. A. Porter, *Testing the Origin of High-energy Cosmic Rays*, *ApJ* **752** (June, 2012) 68, [[1108.1023](#)].
- [77] T. A. Porter and A. W. Strong, *A New estimate of the Galactic interstellar radiation field between 0.1 microns and 1000 microns*, in *29th International Cosmic Ray Conference*, 7, 2005, [astro-ph/0507119](#).
- [78] N. Weinrich, Y. Génolini, M. Boudaud, L. Derome and D. Maurin, *Combined analysis of AMS-02 (Li,Be,B)/C, N/O,  $^3\text{He}$ , and  $^4\text{He}$  data*, *Astron. Astrophys.* **639** (2020) A131, [[2002.11406](#)].
- [79] P. D. L. T. Luque, M. N. Mazziotta, F. Loparco, F. Gargano and D. Serini, *Markov chain Monte Carlo analyses of the flux ratios of B, Be and Li with the DRAGON2 code*, *JCAP* **07** (2021) 010, [[2102.13238](#)].
- [80] J. Heisig, M. Korsmeier and M. W. Winkler, *Dark matter or correlated errors: Systematics of the AMS-02 antiproton excess*, *Phys. Rev. Res.* **2** (2020) 043017, [[2005.04237](#)].